中國機械工程學刊第四十四卷第五期第 399~411 頁(民國一百一十二年)
Journal of the Chinese Society of Mechanical Engineers, Vol.44, No.5, pp399~411 (2023)

Effect of Fineness Ratio on Hypersonic Thermal Flow past a Spherically Blunted Tangent-Ogive Nose Cone

Feng-Yao Chang*, Yu-Chin Chien**and Huei Chu Weng***

Keywords：hypersonic gas dynamics, shock waves, heat transfer, flow drag, spherical nose, tangent-ogive cone, fineness ratio, detachment distance.

ABSTRACT

In this study, a computational fluid dynamics (CFD) simulation is used to explore the external hypersonic thermal-flow fields and characteristics of a spherically blunted tangent-ogive nose cone. The main purpose is to analyze the influence of the fineness ratio (FR) of the nose cone on the shock wave, velocity, pressure, temperature, and density of the airflow, as well as the drag coefficient of the nose cone at a Mach number of 6 and a bluntness ratio of 5. The numerical results show that the effect of fineness ratio on the shock wave type, shape, and detachment distance is not apparent. In the area of the spherical nose, when the fineness ratio increases, the external airflow velocity increases, and the pressure, temperature, and density decrease, but the gradient values of velocity, pressure, temperature, and density remain unchanged. In the area of the tangent-ogive cone body, when the fineness ratio increases, the external airflow velocity also increases, and the pressure, temperature, and density also decrease; however, the gradient values of velocity, pressure, temperature, and density decrease significantly. With the increase of the fineness ratio, it can also be found that the drag coefficient of the spherically blunted tangent-ogive nose cone decreases. As FR=1, 2, and 3, the drag coefficients are 0.9082, 0.7586, and 0.7356, respectively. The results of this study can be applied to the design of the front part of a hypersonic flying object.

Paper Received February, 2023. Revised May, 2023. Accepted August, 2023. Author for Correspondence: Huei Chu Weng.

* *Ph.D., Department of Mechanical Engineering, Chung Yuan Christian University, Taoyuan 32023, Taiwan, ROC.*

** *Assistant Professor, Department of Intelligent Automation Engineering, National Chin-Yi University of Technology, Taichung 411030, Taiwan, ROC.*

** *Professor, Department of Mechanical Engineering, Chung Yuan Christian University, Taoyuan 32023, Taiwan, ROC.*

INTRODUCTION

When a flying object flies at hypersonic speed, the surface of the object will stand high flow drag and heating. Therefore, when designing a hypersonic flying object, it is important to investigate the influence of its appearance on the external thermal-flow fields and characteristics. The drag coefficient of a sharp nose cone is low, but its heat flux is high, so the sharp nose cone is not suitable for the design of the leading edge of a hypersonic flying object. In contrast, a blunt nose cone can generate a normal shock wave when flying at hypersonic speeds, which heats the ambient air, thereby reducing the heat flux on the object surface. Therefore, the blunt nose cone is suitable for the design of the leading edge of a hypersonic flying object. There are many different types of blunt nose cones. Two common types include spherically blunted nose cone and elliptically blunted nose cone. Compared with the geometric shape of the common nose cone with the same fineness ratio, the spherically blunted tangent-ogive nose cone has a larger vertex angle, which can provide more space to install avionics. This type of blunt nose cone is usually used in the front structure of high-speed flying object such as a rocket, an aircraft, and a reentry vehicle in hypersonic flight. In general, the thermal-flow fields and characteristics over a spherically blunted tangent-ogive nose cone are influenced by the geometrical factors, which include the nose cone shape, the fineness ratio, and the bluntness ratio. Previous studies on the effects of these geometrical factors on the thermal-flow fields and characteristics shown in the literature are discussed as follows.

To investigate the effect of fineness ratio on the drag coefficient of a nose cone in the subsonic regime, Aguilar et al. (2015) conducted a numerical study on subsonic flow over a high-power nose cone and an ellipsoid nose cone respectively at a Mach number of 0.75. It was founded that the drag coefficient decrease at the beginning as the fineness ratio increases, until the fineness ratio is equal to 3. When the fineness ratio is greater than 3, the drag coefficient increases as the fineness ratio increases. In the supersonic regime, Saw and Al-Obaidi (2013) did a numerical investigation on the flow past a pointed conical nose cone at Mach number from 2 to 5 and studied the effect of fineness ratio on the drag coefficient of the nose cone. The result revealed that the total drag coefficient decreases as the fineness ratio increases at a constant Mach number. Moreover, O'Brien (2014) did a numerical investigation of drag on the LV Haack and LD Haack nose cones through the subsonic and supersonic regimes. It was found that the drag coefficient is mainly a function of the fineness ratio. In the subsonic regime, the total drag increases as the fineness ratio increases because the viscous drag is predominant in the subsonic regime. On the other hand, in the supersonic regime, the total drag decreases as the fineness ratio increases because pressure drag is predominant in the subsonic regime. To study the influence of fineness ratio on determining minimum-drag shapes, Sahai et al. (2014) conducted a numerical study using a shape optimization framework. The study showed that the optimal axisymmetric body at a given free stream Mach number is blunt-nosed for smaller fineness ratios and sharp or pointed for larger fineness ratios. Narayan et al. (2018) numerically investigated the influence of fineness ratio on the aerodynamic characteristics of spherically blunted nose cones and parabolic nose cones at a Mach number of 5.8. It was found that the spherically blunted nose cone furnishes minimum drag as the fineness ratio is less than 1.2. When the fineness ratio is greater than 1.2, the parabolic nose cone provides superior drag reduction. As to the effect of bluntness on the shock wave, Machell (1956) did an experimental investigation and concluded that the spherical nose governs the shock shape for the spherically blunted nose cones with high bluntness ratios. Relatively, the conical afterbody governs the shock shapes for the spherical nose cones with low bluntness ratios. Furthermore, it was also found from the experimental results that the bow shock detachment distance is varied linearly with the spherical nose radius. To study the influence of bluntness on the drag of the spherical nose cone, Owens (1965) did an experimental investigation on the influence of bluntness on the forebody drag of the spherical nose cone at Mach number from 0.5 to 5. It was observed that the effect of bluntness on the drag coefficient of forebody is large at relatively higher Mach numbers, but the effect of bluntness on the drag coefficient of forebody is small at relatively lower Mach numbers. Hemateja et al. (2017) also numerically studied the influence of nose radius on the drag of the blunt nose cone in supersonic and hypersonic flows. It was observed that the drag of the blunt nose cone increases as the nose radius increases. Rajput et al. (2017) did a numerical investigation on the influence of ogive radius on the drag of the blunted tangent-ogive nose cone under a fixed bluntness ratio. It was also found that the drag coefficient decreases with the increase in the ogive radius. Narayan et al. (2020) did a computational investigation for studying the influence of bluntness and semi-cone angle on the drag of a spherically blunted nose cone at a Mach number of 5.8. It was observed that the smaller bluntness ratio and semi-cone angle are essential for a spherically blunted nose cone to obtain a minimum drag coefficient. In addition, it was also found that the surface heat flux decreases when the bluntness ratio increases and the shock detachment distance is primarily a function of bluntness ratio. To study on the effect of bluntness on the intensity of aerodynamic heating, Harshavardhan et al. (2014) did a numerical investigation on the computational flow analysis of hypersonic reentry blunt vehicle. It was concluded that the aerodynamic heating is reduced by a strong shock wave, which is created by the bluntness of the nose cone. To study the effect of geometrical shape on the temperature distribution at a Mach number of 5 with zero angle of attack, Hussein et al. (2019) did a numerical and comparative study. It was discovered that the heat distribution of temperature for a spherically blunted tangent-ogive nose cone is less than that for a spherical nose cone about 3%. To build the mathematical formulas on the shock detachment distance of a spherically blunt body, Hu et al. (2017) conducted a numerical investigation on the shock detachment distance of hypersonic vehicles at the altitude of 25 km to 55 km and studied the influencing factors about the detachment distance. With the least-squares fitting method, a square polynomial formula was established for the shock detachment distance. This mathematical formula showed that the detachment distance can be estimated with three influence variables, which are the Mach number, the radius of a blunt body, and the altitude in the atmosphere. Similarly, Hornung et al. (2019) conducted a numerical investigation on the sphere and cone behavior of hypersonic flow past a spherically blunted cone and studied the influence factors on the dimensionless shock detachment distance and the drag coefficient. With the hypersonic similarity approach, two mathematical formulas with density ratio and cone angle parameters were built for the dimensionless shock detachment distance and the drag coefficient, respectively. Balaji and Muruga (2020) did a numerical study of the hypersonic flow past different bluff bodies at a Mach number of 5. Their study revealed that the spherically blunted conical shape has better aerodynamic performance. Recently, Chang and Weng (2022) performed a numerical investigation to understand the effect of bluntness ratio on the hypersonic thermal flow past a spherically blunted tangent-ogive nose cone. The results showed that the bluntness ratio factor will lead to a change in shock wave type and shape. The shock detachment distance, the shock layer thickness, and the shock wave strength will increase as the bluntness ratio factor increases. Schramm et al. (2023) conducted experimental and numerical investigations of the hypersonic flow past spherically blunted cone capsules. Their study constructed a theoretical model for the density profile along the stagnation streamline.

Referring to the past literatures, it was found that geometrical factors have a large influence on the aerodynamic characteristics produced by the flying objects. In the field of research, the studies on blunt nose cones mainly focused on spherical blunt nose cones, and less studies on spherically blunted tangent-ogive nose cones. Moreover, the fineness ratio of a spherically blunted tangent-ogive nose cone is one of the geometrical factors that affect the hypersonic thermal-flow fields and characteristics around the nose cone. For general flying objects, the fineness ratio is also an important factor to increase the lift, decrease the drag, and upgrade the aerodynamic efficiency. Therefore, this study using a computational fluid dynamics simulation to analyze the influence of the fineness ratio of a spherically blunted tangent-ogive nose cone on the shock wave, velocity, pressure, temperature, and density of the airflow, as well as the drag coefficient of the nose cone at a hypersonic Mach number. It is hoped that the results of this study can be applied to the design of high-speed flying objects, help to improve the flight performance, and reduce the aerodynamic heating.

In this study, the research background, motivation and aim are introduced in the first section. Then, the geometric model building, meshing and boundary condition setting, and numerical operation are explained in the second section. The numerical validation, and results and discussion are conducted in the third section. Finally, the conclusions are made in the fourth section.

NUMERICAL SETTING

In this study, a computational fluid dynamics (CFD) simulation was applied to do the numerical investigation on the effect of fineness ratio on the hypersonic thermal flow past a spherically blunted tangent-ogive nose cone. In the process of numerical computation, firstly, the geometric model was built by ANSYS Fluent software, then the structure meshing was created, boundary conditions was defined, CFD solver was selected, the viscous model was determined, and finally the results were obtained in the performance of simulation operation. The method used in this study is described as follows.

Geometric Model

The surface of the nose cone can be divided into three areas of spherical nose, tangent-ogive cone body, and base, as shown in Fig. 1. In the research process, the bluntness ratios (BR) of the tangent-ogive cone body were maintained at 0.5; that is, the radius of spherical nose area and the base radius of tangent-ogive cone body were kept at a fixed length. Their values are 0.95 m and 1.9 m, respectively. The surface of the tangent-ogive cone body area was still maintained in the tangent-ogive shape. The only geometrical factor changed in this study is the fineness ratio (FR) of the spherically tangent-ogive nose cone, which is the ratio of the height from the bottom of the nose cone to the top of the nose cone (L) to the base diameter of the nose cone (D). Five FR values of 1.00, 1.50, 2.00, 2.50, and 3.00 were used in this study, as shown in Fig. 2. It could be found that the surface curvature of the tangent-ogive cone body becomes smaller and the arc length of the spherical nose region gets longer as the value of FR increases.

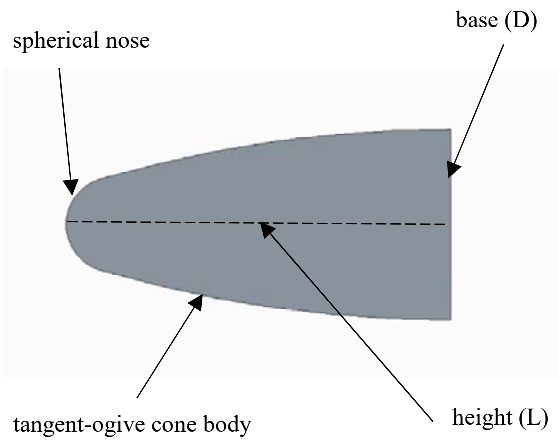

Fig. 1. Geometric sketch of the spherically blunted tangent-ogive nose cone.

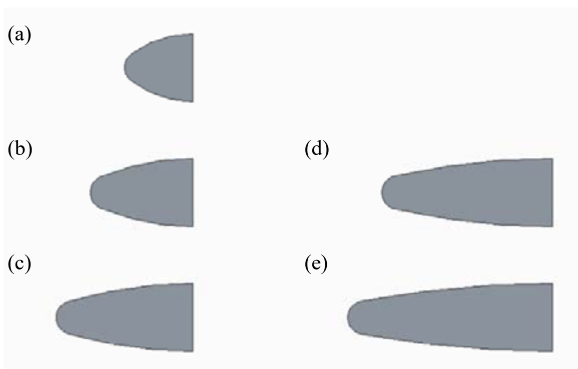

Fig. 2. Cone geometry used in calculations: (a) FR=1.0; (b) FR=1.5; (c) FR=2.0; (d) FR=2.5; (e) FR=3.0.

Structured Mesh

In order to obtain the higher accuracy results in the calculations, a structured mesh was used in this study, as shown in Fig. 3. The areas near the spherical nose and the surface around the tangent-ogive cone body are relatively important areas. The meshing is made by smooth transition, which makes the mesh near the spherical nose and the tangent-ogive cone wall finer. It should be noted that the finest grid size near the wall is about 1.09 cm and that all wall boundary conditions are set as no-slip conditions. In this study, five spherically blunted tangent-ogive cone models with different fineness ratios were used, and the meshing in each model was made by the same method and scale. As a result, the longer fineness ratio of the nose cone model is, the more nodes and meshes it has. The total number of nodes and elements used in this study are 61,680 to 88,591 and 61,200 to 87,880, respectively. As to the quality of mesh, the average skewness is 2.607e-002 to 3.768e-002 and the average orthogonal quality is 0.9946 to 0.9961. These statistics show that the mesh quality in this study is maintained well.

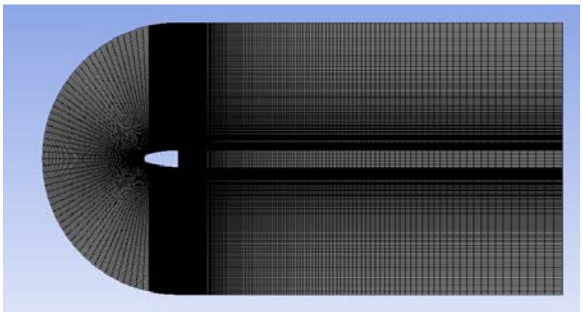

Fig. 3. Structured mesh over the geometry and the domain.

Boundary Conditions

Figure 4 shows the boundary condition settings in this study. The 'inlet', 'far field 1', 'far field 2', and 'outlet' were set as pressure far field condition. Owning to no velocity-slip and the temperature-jump conditions on the nose cone surface, the 'wall' was set as wall condition. Table 1 shows the input values of the pressure far-field, such as temperature, gauge pressure, density, velocity (Mach number), and viscosity coefficient.

Table 1. Input values in the pressure far field.

Temperature (K)	Static pressure (Pa)	Density (kg/m^3)	Velocity (Mach number)	Viscosity (kg/m·s)
300	0	1.176674	6	1.7894x10^{-5}

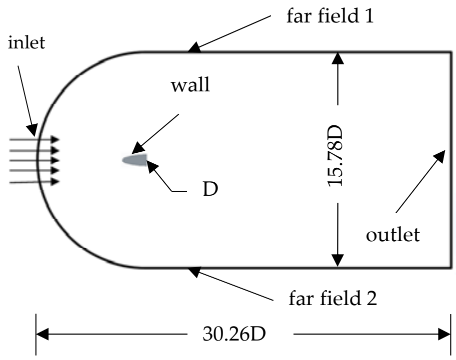

Fig. 4. Boundary condition settings.

Numerical Operation

The numerical computation in this study is a two-dimensional steady-state simulation. The density-based solver is set up to solve the compressible and hypersonic airflow problem. The viscous model adopted is the Spalart-Allmaras model (SA model), which is a one-equation model used to solve the kinematic eddy turbulent viscosity problem. The basic transport equation for the transported variable $\tilde{v}$ is written as:

$$\frac{\partial}{\partial x_i}\left(\rho\tilde{v}u_i\right)=\frac{1}{\sigma_{\tilde{v}}}\left[\begin{array}{l}\dfrac{\partial}{\partial x_i}\left\{\left(\mu+\rho\tilde{v}\right)\dfrac{\partial\tilde{v}}{\partial x_i}\right\}\\ +C_{b2}\rho\left(\dfrac{\partial\tilde{v}}{\partial x_j}\right)^2\end{array}\right] +G_v-Y_v+S_{\tilde{v}} \tag{1}$$

where the first term on the right hand side of the above equation is the diffusion term, G_v is the production of turbulent viscosity, Y_v is the destruction of turbulent viscosity, and $S_{\tilde{v}}$ is a user-defined source term. $\sigma_{\tilde{v}}$ and C_{b2} are the constants. The SA model is suitable for the computation of external flow and turbulent boundary layer flow in aeronautical application. Especially, it is very effective to calculate the external flow field of 2D aircraft with simple geometry. The wall function can also be employed by the SA model when the meshing accuracy is not high (Spalart and Allmaras, 1992). Comparing with the other viscous models, the SA model is a model that can save computer resources in the ANSYS Fluent software. On the other hand, the air fluid is set as an ideal gas. The ideal gas law is written as

$$p=\rho RT \tag{2}$$

where, p is the pressure, ρ is the density, R is the gas constant, and T is the temperature. The setting of air viscosity coefficient is governed by Sutherland's law, which is applicable to a wide temperature range and suitable for the calculation of hypersonic viscous flow (Anderson, 2006). Sutherland's law can be expressed as

$$\mu=\mu_r\left(\frac{T}{T_r}\right)^{3/2}\frac{T_r+S}{T+S} \tag{3}$$

where, μ is the viscosity, T_r is the reference temperature, μ_r is the viscosity at the reference temperature, and S is the Sutherland temperature. Thus, the changes in density and viscosity with temperature variation are governed by the ideal gas law and Sutherland's law, respectively.

RESULTS AND DISCUSSION

The following simulation results are obtained through CFD computation under the conditions of a bluntness ratio of 0.5 and the airflow velocity at a Mach number of 6. The FR ranges from 1 to 3. With the computation results, a numerical validation was finished, and the analysis was performed as follows.

Numerical Validation

In order to verify the rationality of the simulation technology used in this study, a blunted nose cone (BR=0.5, FR=1.32), whose shape and size are similar to the one used by Harshavardhan et al. (2014) is employed in this study. Under the same conditions in the literature, the numerical computation at a Mach number of 6 is carried out by the above-mentioned technology to obtain the static pressure distribution and static temperature distribution of the external airflow along the nose cone surface, as shown in Fig. 5 and Fig. 6, respectively. These figures show that the present results of this study are similar to those in the literature, and the maximum percentage error in static temperature is 6.55%. In addition, Fig. 7 shows the grid independence test on the blunted nose cone with the pressure coefficient (C_p). The value of maximum pressure coefficient $C_{p,\max}$ in the present study is 1.84, obtained from

$$C_{p,\max}=\frac{\gamma+3}{\gamma+1}\left(1-\frac{2}{\mathrm{M}_\infty^{\,2}(\gamma+3)}\right) \tag{4}$$

where γ is the specific-heat ratio and M_∞ is the Mach number of free stream, which approaches the theoretical value 1.81, shown in Harris (1967), with a percentage error of 1.66%. The comparison of these computation results shows that the CFD technology used in this study is quite reasonable. Note that four sets of grids with different cell numbers (28,000, 44,200, 61,200, and 90,700) have been tested, and a cell number of 61,200 used in this study has been shown to be enough to ensure that the numerical solutions are independent.

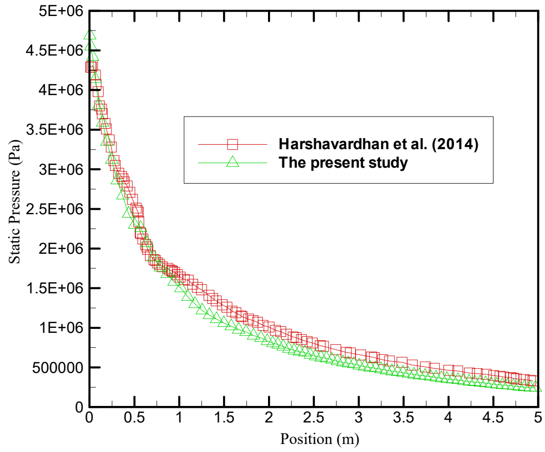

Fig. 5. Comparison of the present results of static pressure with those reported in the literature.

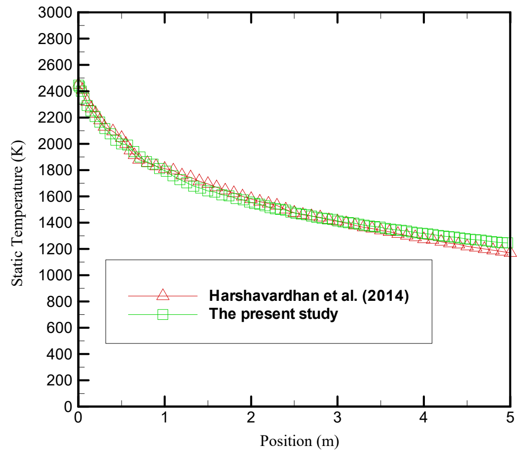

Fig. 6. Comparison of the present results of static temperature with those reported in the literature.

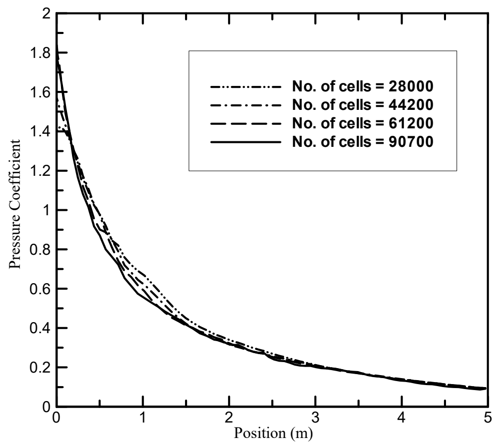

Fig. 7 Variation in pressure coefficient on blunted nose cone with different cell numbers.

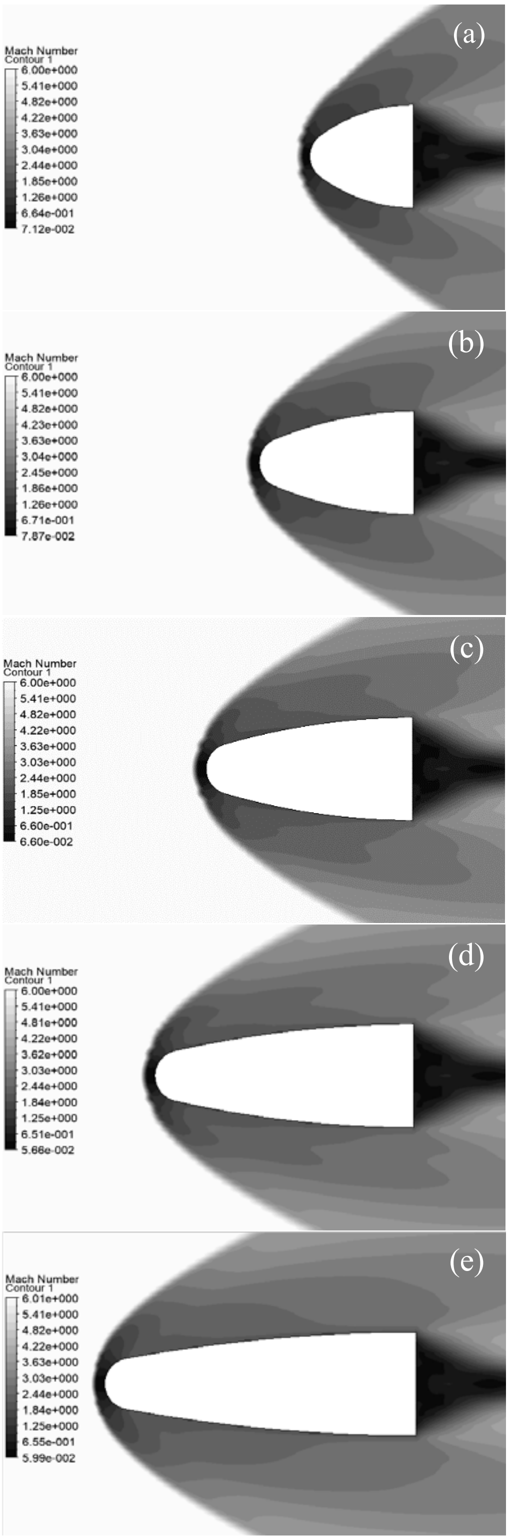

Fig. 8. Mach number contour: (a) FR=1.0; (b) FR=1.5; (c) FR=2.0; (d) FR=2.5; (e) FR=3.0.

FR Effect on Shock Wave

Figure 8 shows the relationship between the shock wave and the fineness ratio FR of the spherically blunted tangent-ogive cone. When the value of FR increases from 1 to 3, the shock wave around the nose cone is still maintained a detached shock wave. The shock detachment distance and the shock wave shape are not be changed with the increase in FR significantly. These results show that under the condition of fixed values of BR and Mach number, the shock wave type, shock detachment distance, and shock wave shape are not changed with the variation of FR significantly. The main reason for such results can be realized from the relevant equations for the coordinate of the shock listed in Billig (1967). It can be known from the literature that the spherical nose radius and airflow Mach number are the main factors that affect the shock detachment distance and shock wave shape.

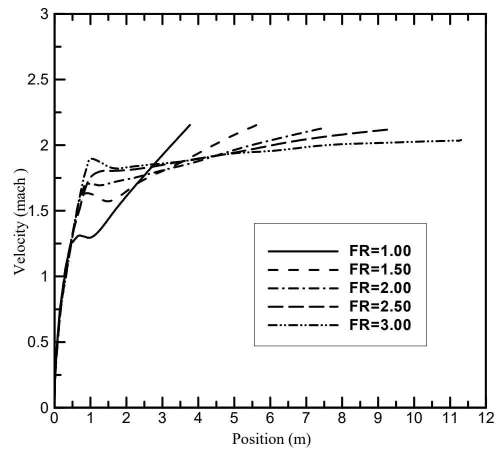

Fig. 9. Velocity distribution over the nose cone for different values of FR.

FR Effect on Airflow Velocity

Figure 8 also shows the relationship between the airflow velocity around the nose cone and FR. From the CFD computation results, it can be found that the airflow passing through the shock wave is compressed by the shock wave and its velocity is sharply slowed down. The airflow velocity at the center of the nose cone is close to the Mach number of 0, indicating that the stagnation point appears in front of the center of the blunt nose cone. As shown in Fig. 8, the black (or dark gray) regions are very low velocity areas, where the airflow velocity are below a Mach number of 0.671. With the increase in FR, the size of black (or dark gray) regions does not change significantly. After the airflow leaves the center of the nose cone, it will flow around the convex surface along the surface of the spherical nose area and the surface of tangent-ogive cone body area, and then generate a series of expansion waves, which further accelerate the flow of airflow downstream. The airflow accelerates along the edges of the nose cone due to the expansion wave effect, as shown in

Fig. 9. Since the airflow velocities in the spherical nose area and the tangent-ogive cone body area are approximately linearly related to the position in the axis direction, a simple average method can be used to calculate the average velocity gradient of airflow in Table 2. This velocity distribution also shows that the airflow velocity can be accelerated to a lower value as FR increases; the airflow velocity gradient in the spherical nose area is greater than that in the tangent-ogive cone body area due to the strong shock curvature in the spherical nose area. In the spherical nose area, the airflow velocity gradient is not be changed with the variation of FR significantly due to this area with a spherical surface, as shown in Table 2. However, since the nose cone with a larger value of FR provides a larger range of spherical surface for air-flow acceleration, the airflow velocity can be accelerated to a higher value in this area. The highest airflow velocity is equal to 1.31 mach when FR=1 and reaches 1.89 mach as FR is 3. Relatively, in the tangent-ogive cone area, a larger value of FR provides a smaller of the convex surface curvature. Therefore, the expansion wave effect is relatively weakened, making the airflow velocity gradient smaller and the airflow acceleration slower. The nose cone with a larger value of FR has a smaller air velocity gradient due to the smaller curvature of convex surface and expansion wave effect, as shown in Table 2. Therefore, the airflow can be accelerated to a lower velocity in this area as FR increases. In the tangent-ogive cone area, the highest airflow velocity is equal to 2.15 mach as FR=1 but only reaches 2.04 mach when FR is 3. Furthermore, for the value of FR increases from 1 to 3, the airflow around the junction of the spherical nose and tangent-ogive cone body expands overly, and then the velocity drops significantly to an equilibrium value.

Table 2. Average velocity gradient of airflow in the spherical nose area and tangent-ogive cone body area for different values of FR.

Location / FR	Spherical nose	Tangent-ogive cone body
1.0	1.7227	0.3076
1.5	1.7279	0.1424
2.0	1.7352	0.0704
2.5	1.7096	0.0411
3.0	1.8003	0.0226

Unit: mach/m

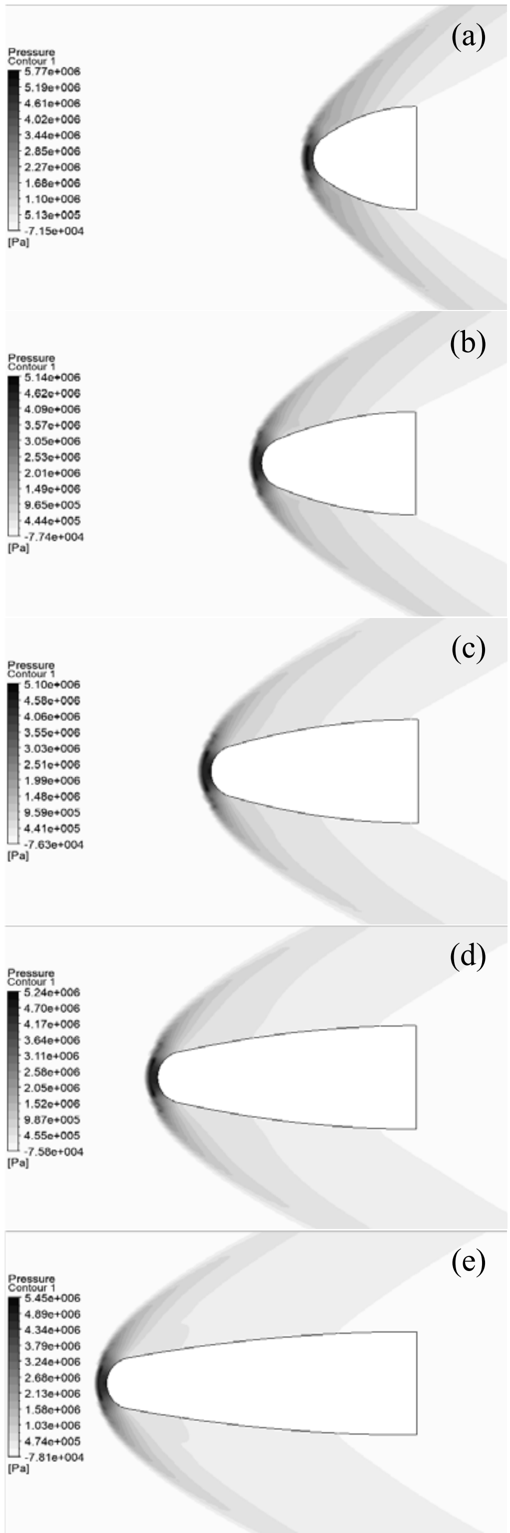

Fig. 10. Static pressure contour: (a) FR=1.0; (b) FR=1.5; (c) FR=2.0; (d) FR=2.5; (e) FR=3.0.

FR Effect on Pressure

Figure 10 shows the relationship between the static pressure of the airflow around the nose cone and FR. The computation results reveals that the static pressure of the airflow behind the shock wave increases sharply due to the airflow compressed by the shock wave, and reaches the maximum value in front of the center of the nose cone. Then, the airflow leaves the center of the nose cone and moves along the edge of the nose cone. The static pressure of airflow decreases rapidly due to the expansion wave on the convex surface of the nose cone. As shown in Fig. 9, the black (or dark gray) regions are the areas with extremely high air static pressure, which are about 4.58e+006 Pa to 5.77e+006 Pa, but their ranges do not expand significantly as FR increases. The static pressure distribution shown in Fig. 11 and the static pressure gradient shown in Table 3 reveal that the static pressure of the airflow can be reduced to a lower value as FR increase; the static pressure gradient in the spherical nose area is greater than that in the tangent-ogive cone body area due to the strong shock curvature in the spherical nose area. In the spherical nose area, the static pressure gradient of airflow is not changed with the variation of FR significantly due to the spherical surface factor, as shown in Table 3. As FR increases, the static pressure will be decreased to a lower value due to the larger range of expansion wave in this area. The lowest static pressure of the airflow is equal to 1.59e+006 Pa when FR=1 and is decreased to 4.87e+005 Pa as FR is 3. Comparably, in the tangent-ogive cone body area, the nose cone with a larger value of FR has a smaller static pressure gradient due to the smaller curvature of convex surface and expansion wave effect, as shown in Table 3. In the tangent-ogive cone area, the lowest static pressure of the airflow is equal to 2.93e+005 Pa as FR=1 and will drop to 1.27e+005 P when FR is 3. Furthermore, owing to the overexpansion, the airflow pressure around the junction portion of the spherical nose and tan-gent-ogive cone body decreases overly and then increases to an equilibrium value as the value of FR increases from 1 to 3 (Machell, 1956).

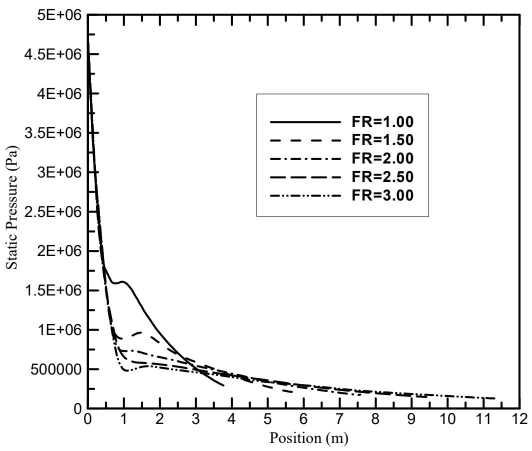

Fig. 11. Static pressure distribution over the nose cone for different values of FR.

Table 3. Average static pressure gradient of airflow in the spherical nose area and the tangent-ogive cone body area for different values of FR.

FR \ Location	Spherical nose	Tangent-ogive cone body
1.0	-4.2901E+06	-4.7180E+05
1.5	-4.1795E+06	-1.8124E+05
2.0	-4.1563E+06	-8.9495E+04
2.5	-4.0735E+06	-5.5334E+04
3.0	-4.1014E+06	-4.2935E+04

Unit: Pa/m

FR Effect on Temperature

Figure 12 shows the relationship between the static temperature of airflow around the nose cone and FR. The results in these figures show that the shock wave layer behind the shock wave and the hypersonic boundary layer around the nose cone become high static temperature areas of airflow. Especially, the black (or dark gray) regions in these figures are the extremely high static temperature areas, which are about 2240 K-2450 K. With the increase in FR, the black (or dark gray) regions of the shock wave layer behind the shock wave do not significantly expand. It is also found from the results that the static temperature of airflow in the shock wave layer and the hypersonic boundary layer increase sharply due to the conversion of kinetic energy of the airflow to the internal energy of the airflow.

After leaving the center of the nose cone, the airflow accelerates along the edge of the nose cone, and so the internal energy of the airflow is converted into kinetic energy, which makes the static temperature of airflow drop, as shown in Fig. 13. This static temperature distribution diagram also shows

Table 4. Average static temperature gradient of airflow in the spherical nose area and the tangent-ogive cone body area for different values of FR.

FR \ Location	Spherical nose	Tangent-ogive cone body
1.0	-880.52	-202.16
1.5	-947.55	-88.69
2.0	-961.28	-44.04
2.5	-980.10	-25.27
3.0	-1006.58	-14.11

Unit: K/m

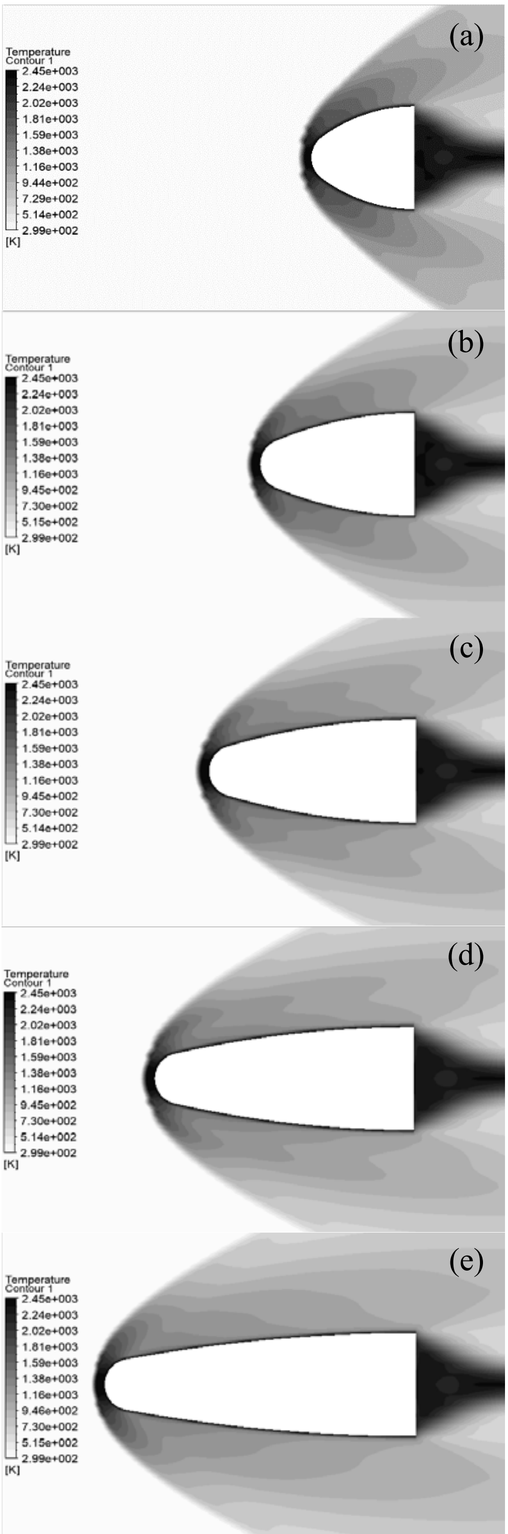

Fig. 12. Static temperature contour: (a) FR=1.0; (b) FR=1.5; (c) FR=2.0; (d) FR=2.5; (e) FR=3.0.

that the static temperature of the airflow can be reduced to a higher value as FR increases. Since the large velocity gradient in the spherical nose area causes strong thermodynamic changes, the static temperature gradient in the spherical nose area is also larger than that in the tangent-ogive nose cone area. Similarly, in the spherical nose area, the static temperature gradient of airflow is relatively fixed and not be changed with the variation of FR significantly due to the spherical surface factor, as shown in Table 4. As FR increases, the static temperature will be reduced to a lower value due to the larger range for the expansion and acceleration of the airflow in this area. The lowest static temperature of the airflow is equal to 1826 K when FR=1 and drops to 1428 K as FR is 3; in the tangent-ogive cone area, the nose cone with a larger value of FR has a smaller temperature gradient due to the smaller curvature of convex surface and expansion wave effect, as shown in Table 4. In the tangent-ogive cone area, the lowest static temperature of the airflow drops to 1275 K as FR=1 but only drops to 1341 K when FR is 3. In addition, when the value of FR increases from 1 to 3, the airflow temperature around the junction portion of the spherical nose and tangent-ogive cone body decreases overly and then increases to an equilibrium value due to the airflow overexpansion.

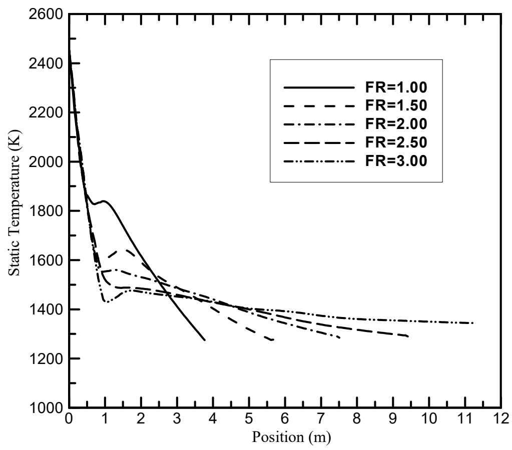

Fig. 13. Static temperature distribution over the nose cone for different values of FR.

FR Effect on Density

Figure 14 also shows the relationship between airflow density around the nose cone and FR. The CFD computation results discover that the airflow density passing through the shock wave rapidly increases due to the compression of the shock wave and reaches the maximum value in front of the center of the nose cone. The black (or dark gray) regions in these figures represent relatively high-density regions, which is about 6.65 kg/m^3 to 8.56 kg/m^3. When leaving the center of the nose cone, the airflow flows downstream along the edge of the nose cone, and its density gradually decreases, as shown in Fig. 15. This density distribution diagram also shows that the

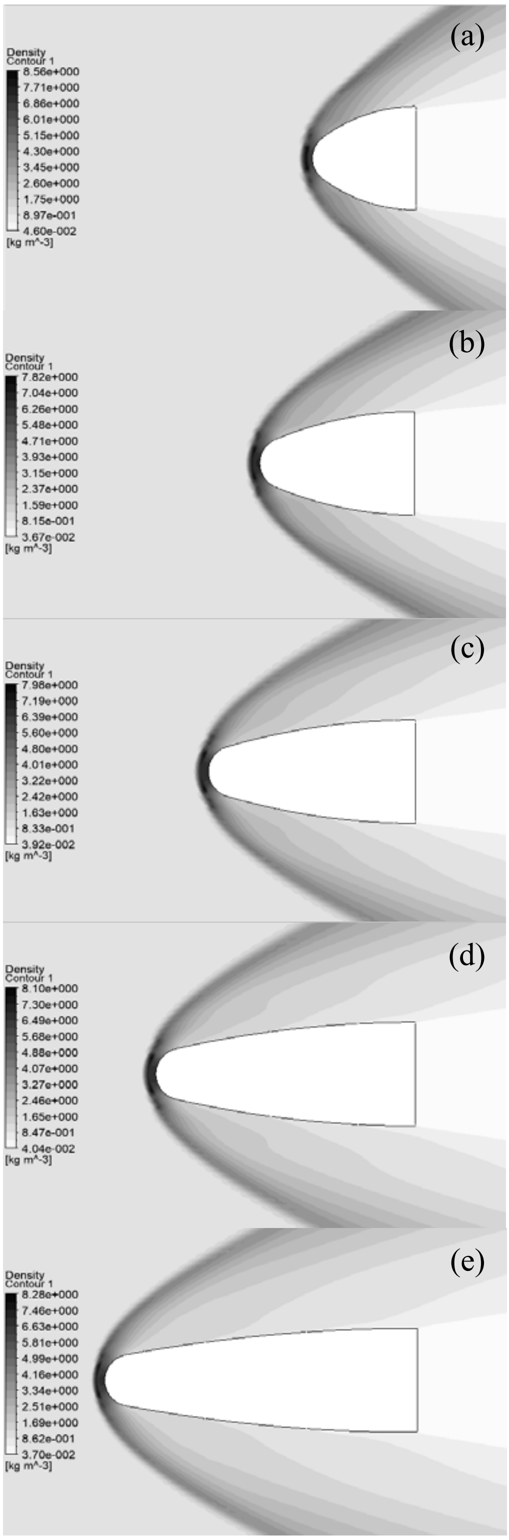

Fig. 14. Density contour: (a) FR=1.0; (b) FR=1.5; (c) FR=2.0; (d) FR=2.5; (e) FR=3.0.

density of the airflow can be reduced to a lower value as FR increase. Similarly, the airflow density gradient in the spherical nose area is greater than that in the tangent-ogive cone body area due to the strong shock in around the spherical nose area. In the spherical nose area, the airflow density gradient is relatively fixed and not be influenced by the change of FR significantly due to the spherical surface factor, as shown in Table 5. As FR increases, the airflow density will be reduced to a lower value due to the larger range for the expansion in this area. The lowest airflow density is equal to 3.22 kg/m^3 when FR=1 and will be decreased to 1.43 kg/m^3 as FR is 3. In the tangent-ogive cone body area, as FR increase, the airflow density gradient becomes smaller, and the decrease of airflow density slows down due to the smaller convex surface curvature in this area, as shown in Table 5. In the tangent-ogive cone body area, the lowest airflow density is equal to 1.07 kg/m^3 when FR=1 and will be reduced to 0.59 kg/m^3 as FR is 3. When the value of FR increases from 1 to 3, the airflow overexpansion around the junction portion of the spherical nose and tangent-ogive cone body also causes the density to decrease overly and then are increased to an equilibrium value.

Table 5. Average density gradient of airflow in the spherical nose area and tangent-ogive cone body area for different values of FR.

FR \ Location	Spherical nose	Tangent-ogive cone body
1.0	-4.9478	-0.7754
1.5	-5.0999	-0.3421
2.0	-5.1792	-0.1788
2.5	-5.1154	-0.1182
3.0	-5.2400	-0.0956

Unit: kg/m^4

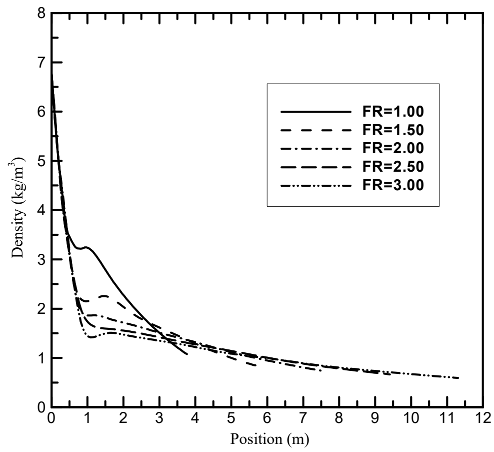

Fig. 15. Density distribution over the nose cone for different values of FR.

FR Effect on Drag Coefficient

Figures 16 to 18 show the relationship between the drag coefficients and FR. The CFD computation results shows that the total drag of the nose cone mainly comes from pressure drag and a very small proportion comes from viscous drag. When FR=1, the total drag coefficient C_d is equal to 0.9082. Then the drag coefficient of the nose cone decreases as FR increases. As the value of FR is 3, the total drag coefficient C_d is 0.7356. When the value of FR is between 1 and 2, C_d decreases significantly; after the value is greater than 2, C_d decreases slowly, as shown in Fig. 16. Of the total drag coefficient C_d, the pressure drag coefficient C_{dp} also decreases with the increase in FR because the nose cone becomes slender, as shown in Fig. 17. However, as FR increases, the surface area of the nose cone increases, so the viscous drag coefficient C_{dsf} increases instead, as shown in Fig. 18.

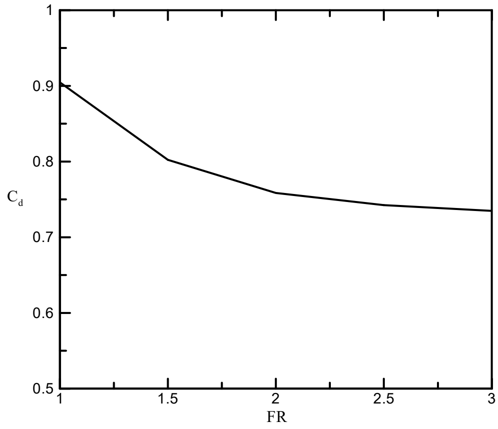

Fig. 16. Total drag coefficient with varying FR.

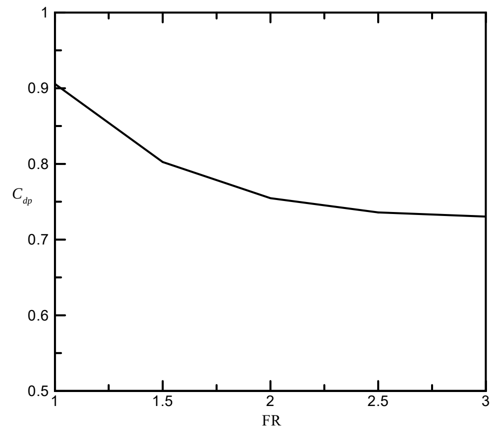

Fig. 17. Pressure drag coefficient with varying FR.

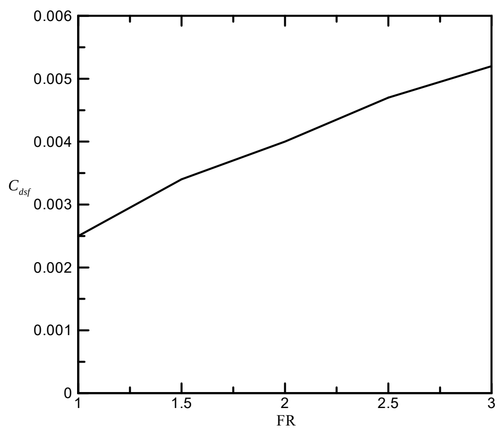

Fig. 18. Viscous drag coefficient with varying FR.

CONCLUSIONS

In this study, a numerical computation has been carried out to explore the hypersonic thermal-flow fields and characteristics of external airflow around a spherically blunted tangent-ogive nose cone at a Mach number of 6 and a bluntness ratio of 5. The effect of fineness ratio was investigated to understand the influence of various fineness ratios (1, 1.5, 2, 2.5, and 3) on the shock wave, pressure, temperature, density, velocity, and drag coefficient of the airflow around the nose cone. Finally, through comprehensive analysis and discussion, the main results are obtained, which are summarized as follows:

1. The influence of the change in fineness ratio on the shock wave type, the shock detachment distance, and the shock wave shape is not so apparent due to the fixed values of the bluntness ratio and the Mach number.
2. The change in the fineness ratio can affect the airflow velocity, static pressure, static temperature, and density distribution around the nose cone. With the increase in fineness ratio, the static pressure, static temperature, and density can be reduced to lower values, but the airflow speed can be increased to a higher value due to the spherical surface factor in the spherical nose area and the smaller convex surface curvature in the tangent-ogive cone body area.
3. The total drag coefficient of the spherically blunted tangent-ogive nose cone mainly comes from the pressure drag coefficient, and a very small part of the total drag coefficient comes from the viscous drag coefficient. With the increase in fineness ratio, the pressure drag coefficient decreases, but the viscous drag coefficient increases. As a result, the total drag coefficient also decreases as the fineness ratio increases.

ACKNOWLEDGMENT

This work was financially supported by the National Science and Technology Council of Taiwan under Grant No. MOST 111-2221-E-033-037-.

REFERENCES

Aguilar, G., Balogun, G., Canchola, S., Chinnery, L., Doddanavar, R., Hudgins, J., Kneese, A., Liggett, J., Marcotte, E., Myers, C., O'Neil, M., Pages, A., Pasket, J., Pettit, J., Recchia, S., Revak, T., Sandman, T., Savage, D., Stahl, J., Stricklin, B., Venesky, M., Wakefield, J., and Ward, D., *SRT-2 Phoenix*, Technical Analysis Report, Texas A&M University (2015).

Anderson, J.D, *Hypersonic and High Temperature Gas Dynamic*, McGraw-Hill (2006).

Billig, F.S., "Shock-wave shapes around spherical and cylindrical-nosed bodies," J. Spacecr. Rockets, Vol.4, No.6, pp. 822-823 (1967).

Balaji R, and Muruga L.J., *Performance analysis on varies bluff bodies at hypersonic speed*, 2020 International Conference on Interdisciplinary CyberPhysical Systems (ICPS), pp. 62-67 (2020).

Chang, F.Y. and Weng, H.C., "Hypersonic thermal flow past a spherically blunted tangent-ogive nose cone," *J. Chin. Soc. Mech.*, Vol.43, No.1, pp. 1-10 (2022).

Harris, J.E., *Aerodynamic Characteristics of Spherically Blunted 250 Cones at Mach Number of 20*, Technical Note, NASA TN D-4098 (1967).

Harshavardhan, N.S., Sanjana, K., Sai Sharan, K., and Srinivas, G., "Computational flow analysis of hypersonic reentry blunt body using Fluent and Gambit," *Int. J. Sci. Eng. Technol. Res.*, Vol.5, No.5, pp. 262-269 (2014).

Hemateja, A., Ravi Teja, B., Dileep Kumar, A., and Rakesh, S.G., "Influence of nose radius of blunt cones on drag in supersonic and hypersonic flows," *IOP Conf. Ser.: Mater. Sci. Eng.*, Vol.225, pp. 012045 (2017).

Hornung, H.G., Schramm, J.M., and Hannemann, K., "Hypersonic flow over spherically blunted cone capsules for atmospheric entry. Part1. The sharp cone and the sphere," *J. Fluid Mech.*, Vol.871, pp. 1097-1116 (2019).

Hu, Y.M., Huang, H.M., and Guo, J., "Shock wave standoff distance of near space hypersonic vehicles," *Sci. China Technol. Sci.*, Vol.60, pp. 1123-1131 (2017).

Hussein, E.Q., Rashid, F.L., and Azziz, H.N., "Aerodynamic heating distribution for temperature prediction of fast flying body nose using CFD," *J. Adv. Res. Fluid Mech. Therm. Sci.*, Vol.64, No.2, pp. 183-195 (2019).

Machell, R.M., *An Experimental Investigation of Hypersonic Flow over Blunt Nosed Cones at a Mach number of 5.8*, Engineer's Thesis, California Institute of Technology (1956).

Narayan, A., Narayanan, S., and Kumar, R., "Hypersonic flow past nose cones of different geometries," *Simul.*, Vol.94, No.8, pp. 665-680 (2018).

Narayan, A., Narayanan, S., Kumar, R., Kumar, C.S., and Jagadeesh, G., "Hypersonic flow past a spherically blunted nose cone: A computational study," *Prog. Comput. Fluid Dyn.*, Vol.20, No.2, pp. 105-123 (2020).

O'Brien, C., *An Investigation of Drag on the Haack Series Nose Cones through Subsonic and Supersonic Mach Regimes*, Honors Thesis, University of Alabama in Huntsville (2014).

Owens, R.V., *Aerodynamic Characteristics of Spherically Blunted Cones at Mach Number from 0.5 to 5.0*, Technical Note, NASA TN D-3088 (1965).

Rajput, B., Pandey, P.K., Narayan, A., and Narayanan, S., "Computational study of supersonic flow past blunted tangent-ogive nose cone," *Int. J. Adv. Res. Sci. Eng.*, Vol.6, No.3, pp. 818-824 (2017).

Sahai, A., John, B., and Natarajan, G., "Effect of fineness ratio on minimum-drag shapes in hypersonic flows," *J. Spacecr. Rockets*, Vol.51, No.3, pp. 900-907 (2014).

Saw, A.S.Q. and Al-Obaidi, A.S.M., *Drag of Conical Nose at Supersonic Speeds*, EUREKA Annual Report, Taylor's University (2013).

Schramm, J.M., Hannemann, K., and Hornung, H.G., "Hypersonic flow over spherically blunted cone capsules for atmospheric entry. Part 2. Vibrational non-equilibrium effects," *J. Fluid Mech.*, Vol.954, A32 (2023).

Spalart, P.R. and Allmaras, S.R., *A One-equation Turbulence Model for Aerodynamic Flows*, American Institute of Aeronautics and Astronautics 92-0439 (1992).

球狀切面尖拱形鼻錐細長比對極音速熱流之影響

張峰垚　　翁輝竹
中原大學機械工程學系

簡育欽
國立勤益科技大學智慧自動化工程系

摘 要

本研究係透過計算流體動力學(CFD)模擬來探索球狀切面尖拱形鼻錐的外部極音速熱流場及特性。主要目的為分析在固定極音速馬赫數 6 和鈍度比 5 下，球狀切面尖拱形鼻錐的細長比(Fineness Ratio，FR)對該鼻錐外部周圍流場的震波、速度、壓力、溫度、密度與阻力係數的影響。數值結果表示，細長比對鼻錐外部流場的震波類型、形狀及離體距離影響不明顯。在球狀鼻部區域，當細度比增加時，外部流場之氣流速度提升，且靜壓、靜溫及密度降低，惟其速度、靜壓、靜溫及密度的梯度值保持不變。在切面尖拱形錐形體區域，當細長比增加時，外部流場之氣流速度提升，且靜壓、靜溫及密度降低；然而，速度、靜壓、靜溫及密度的梯度值具有顯著降低。隨著細長比值增加，球狀切面尖拱形鼻錐之阻力係數減小。當 FR 值為 1、2 及 3 時，其阻力係數分別為 0.9082、0.7586 及 0.7356。